

Accurate Lung Nodule Segmentation with Detailed Representation Transfer and Soft Mask Supervision

Changwei Wang, Rongtao Xu, Shibiao Xu *Member, IEEE*, Weiliang Meng *Member, IEEE*, Jun Xiao *Member, IEEE*, and Xiaopeng Zhang, *Member, IEEE*

Abstract—Accurate lung lesion segmentation from Computed Tomography (CT) images is crucial to the analysis and diagnosis of lung diseases such as COVID-19 and lung cancer. However, the smallness and variety of lung nodules and the lack of high-quality labeling make the accurate lung nodule segmentation difficult. To address these issues, we first introduce a novel segmentation mask named “*Soft Mask*” which has richer and more accurate edge details description and better visualization, and develop a universal automatic *Soft Mask* annotation pipeline to deal with different datasets correspondingly. Then, a novel Network with detailed representation transfer and *Soft Mask* supervision (DSNet) is proposed to process the input low-resolution images of lung nodules into high-quality segmentation results. Our DSNet contains a special Detail Representation Transfer Module (DRTM) for reconstructing the detailed representation to alleviate the small size of lung nodules images, and an adversarial training framework with *Soft Mask* for further improving the accuracy of segmentation. Extensive experiments validate that our DSNet outperforms other state-of-the-art methods for accurate lung nodule segmentation, and has strong generalization ability in other accurate medical segmentation tasks with competitive results. Besides, we provide a new challenging lung nodules segmentation dataset for further studies.

Index Terms—Medical images segmentation, lung nodules segmentation, *Soft Mask*, detailed representation transfer.

I. INTRODUCTION

SINCE December 2019, the world has suffered a severe health crisis: COVID-19 pandemic [1]. COVID-19 usually appears as a ground glass opacity (GGO) lung nodule on computed tomography (CT) images [2]. These GGO and other types of lung nodules potentially contain the risk of lung cancer, which is the deadliest type of cancer worldwide for human with a relatively low five-year survival rate of 18% [3]. Accurate segmentation of the lung nodule is of great significance for automated disease screening, diagnosis, analysis, and treatment evaluation [4], [5]. However, accurate

C. Wang and R. Xu contributed equally. S. Xu and W. Meng are the corresponding authors (shibiaoxu@bupt.edu.cn; weiliang.meng@ia.ac.cn).

C. Wang, R. Xu, W. Meng, J. Zhang and X. Zhang are with School of Artificial Intelligence, University of Chinese Academy of Sciences and National Laboratory of Pattern Recognition, Institute of Automation, Chinese Academy of Sciences. S. Xu is with school of Artificial Intelligence, Beijing University of Posts and Telecommunications. Jun Xiao is with School of Artificial Intelligence, University of Chinese Academy of Sciences.

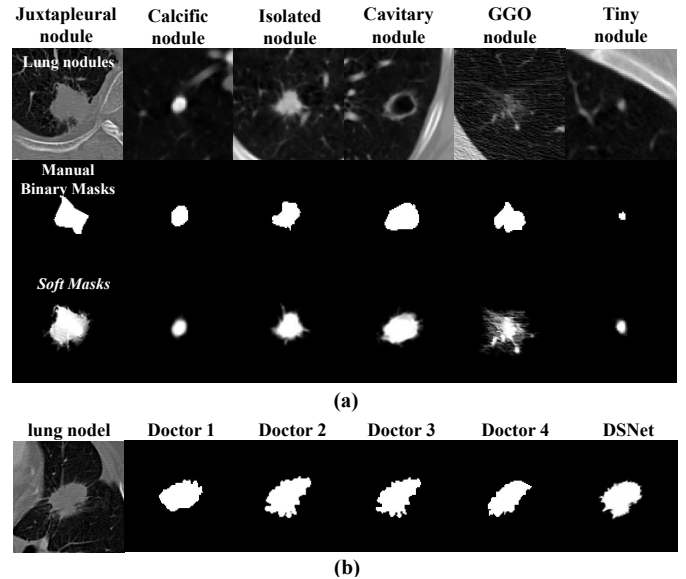


Fig. 1. (a): Various types of lung nodules and manual labelings in LIDC. (b): Comparison of the labeling results of four doctors in LIDC with prediction of our proposed DSNet. Our proposed DSNet even achieves better segmentation and visualization results than human radiologists.

lung nodule segmentation is a challenging problem due to the following various reasons.

“One cannot make bricks without straw” is a commonly used expression to imply that it will be challenging to complete the work without the support of the primary conditions. Unfortunately, this tends to be the case for the current accurate segmentation of lung nodules without high-quality mask annotations. High-quality mask annotation datasets for accurate segmentation of lung nodules are absent, because manually labeling lung nodules mask is a time-consuming work obviously [6], while lung nodules annotation by radiologists is a highly subjective task, often influenced by individual bias and clinical experiences. As shown in Fig. 1 (b), there are apparent differences in the labels of four doctors, and these inconsistencies may cause ambiguities in the segmentation network training. Cai et al. [7] proposed an automatic mask generation method using the long and short axis of RECIST [8] as weakly prior information to avoid manually label the mask, while this is an iterative process, and can only obtain a rough mask by

relying on coarse RECIST marks and GrabCut [9], making it difficult to cope with the task of accurate segmentation of lung nodules with complex edges.

In addition, some inherent characteristics of lung nodules also cause difficulty in their segmentation. On the one hand, lung nodules are usually small ($5 \sim 10$ mm) [4], which leads to the low resolution of the input image. Obviously, low-resolution input loses detailed information of the lesion and makes it difficult to be segmented accurately. On the other hand, as shown in Fig. 1 (a), lung nodules have significant heterogeneity. Some lung nodules such as GGO and burr nodules have irregular shapes and complex edges which also pose challenges for accurate segmentation [10]. However, as shown in Fig. 1, the existing binary mask cannot describe the edge details of these nodules well, so it is difficult to achieve accurate segmentation and visualization in this case.

To address the above issues, we propose an innovative paradigm including a automatic accurate annotation pipeline and a segmentation network named **DSNet** with detailed representation transfer and *Soft Mask* supervision for accurate lung nodules segmentation. Superior to most deep learning-based lung nodules segmentation methods [11]–[14], we not only improve the segmentation network architecture, but also improve the qualities of both the less-explored input (low-resolution images) and ground truth masks (rough binary masks). Specifically, our *Soft Mask* can preserve rich edge details and smooth transition between lung nodules and surrounding pathological environments, making it have a better visualization effect and richer information. And we develop an automatic accurate annotation pipeline to derive accurate *Soft Masks* from different datasets. In addition, inspired by the recently popular self-supervised pre-training model [15], we carefully design a Detailed Representation Transfer Module (DRTM) in DSNet to transfer detailed representation knowledge from an off-the-shelf SRGAN [16] model. It can alleviate the problem of the low resolution of the input images. In general, our technical contributions have the following four aspects:

- We introduce a new fine mask form “*Soft Mask*” and the automatic accurate labeling pipeline, which can boost segmentation accuracy and obtain excellent visualization in contrast to the traditional binary mask.
- We design a novel DSNet with a Detailed Representation Transfer Module and a *Soft Mask* based adversarial training framework to convert low-quality images input into high-quality segmentation results. Unlike most related methods, we improve the quality of the input image and supervision mask that were rarely explored before.
- We propose a special accurate lung nodules segmentation paradigm based on the above innovation, and its performance outperforms other state-of-the-art methods on lung nodules segmentation. In addition, it is also suitable for other accurate medical segmentation tasks after our validation.
- We provide a new lung nodules segmentation dataset (*LNSM*¹) with both *Soft Mask* labelings and binary masks, containing 1500 accurate segmentation nodules.

This work extends our preliminary conference version [17]² in the following aspects. **Firstly**, we provide a general effective medical super-resolution model based on our self-supervised training and apply its detailed representation to promote medical segmentation task (Sec. III-B3 (1)). **Secondly**, we design a novel Detailed Representation Transfer Module to flexibly transfer the detailed information of the super-resolution model into the segmentation pipeline (Sec. III-B3 (2)). **Thirdly**, we increase experimental validation of our method’s robustness and generalization. Specifically, we validate the robustness by comparing models trained on cross-domain datasets with human doctors (Sec. IV-C), then apply to medical segmentation datasets other than lung nodule segmentation to verify the generalization of our method (Sec. IV-D). **Finally**, we also provide a more inclusive and insightful discussion on our method (see Sec. IV-E).

II. RELATED WORK

A. Lung Nodules Segmentation

Many classic hand-craft features based methods have been proposed to deal with lung nodules segmentation, such as morphological operations based methods [18], region-growing methods [19], energy optimization based method [20], [21], Conditional Random Field (CRF) based method [22]. However, these methods cannot cope with lung nodules segmentation well [14], especially for irregular-shaped nodules.

In recent years, deep learning based methods have gained new attention for medical image analysis and processing. Some convolutional neural networks (CNN) based lung nodules segmentation methods [11]–[14] have achieved highly competitive segmentation accuracy. In addition, some other medical segmentation methods [2], [23]–[27] have brought breakthroughs in a variety of medical segmentation tasks. More recently, some transformer-based models [28], [29] are proposed for medical image segmentation. These methods employ more complex network architecture to improve the segmentation accuracy, such as the use of attention mechanisms, spatial context, and dense connections. In contrast, our DSNet not only improves the network structure but also creatively ameliorates the quality and detail of both input images and supervised ground truth to achieve accurate lung nodules segmentation and impressive visualization.

B. Soft Labels

Soft labels have recently been applied to brain lesions segmentation [30], [31] as they are considered to have a better generalization, faster learning speed, and mitigation of network over-confidence. Specifically, Kats et al. [30] employed morphological dilation to expand the binary mask and assigned a fixed probability to all pixels within the expanded region to generate soft labels. Gros et al. [31] obtained soft labels by bilinear interpolation, while they still lost many edge details (e.g. small burrs around lung nodules). Both the soft labels in [30] and [31] softened the binary masks, but they are still

¹It is available at [dataset release].

²It was accepted as oral by ICME 2022 and see the supplementary material for full paper.

too rough to obtain accurate lung nodule segmentation with good visual effects. In contrast, the pixels of our *Soft Mask* are not discrete but continuous, meaning that our *Soft Mask* has richer and more accurate edge detail expression which can reduce the impact of imprecise boundary annotation. Our *Soft Mask* can be obtained from various datasets. In particular, the RECIST marks in the current hospital picture and archiving systems (PACS) can be employed for quick generation of large-scale and high-quality *Soft Masks*.

C. Detailed Representation in Medical images

High-resolution medical images are usually preferred in clinical practice due to more clear image structure and texture details, as well as the benefits to subsequent analysis and processing [32]. These detailed representations in high-resolution images are very important for accurate segmentation, especially in edge regions. Unfortunately, the extremely small lung nodules are difficult to overcome the challenges of hardware, physical and physiological factors to obtain high-resolution images under the existing imaging system. In recent years, some deep learning-based natural images or medical images super-resolution methods [16], [33]–[35] have excellent performance in image resolution improvement. However, the lack of high-resolution training data limits the application of these methods. In addition, the potential of combining these methods with medical segmentation has not been fully exploited. In this work, we conduct self-supervised training on a super-resolution model for medical images and smartly transfer the detailed representation knowledge in the trained super-resolution model to the lung nodule segmentation pipeline.

III. METHODOLOGY

In this section, we propose a complete paradigm for accurate lung nodule segmentation. First, we introduce the *Soft Mask* and develop a pipeline to label it automatically. Then, we design a novel DSNet with detailed representation transfer and *Soft Mask* based adversarial training framework.

A. *Soft Mask* for Lung Nodule Segmentation

1) *Definition of Soft Mask*: Lung nodules are usually labeled and segmented in the form of a binary mask in most methods. However, the binary mask has many disadvantages in accurately segmenting lung nodules. First, it cannot clearly describe the edge and morphological details of the lung nodules, which may cause anatomical information in these marginal regions to be ignored. Second, the labeling is extremely unbalanced since most of the regions are labeled as non-lesion in the binary mask [30], and this imbalance impairs the training of the segmentation network.

To overcome the weakness of the binary mask, we introduce a new form of accurate labeling called *Soft Mask* for lung nodule segmentation inspired by the image matting task [36]. We define the i -th pixel of *Soft Mask* M_i as a linear combination of the lesion label L_i (the value is 1) and non-lesion background label B_i (the value is 0):

$$M_i = \alpha_i L_i + (1 - \alpha_i) B_i, \quad (1)$$

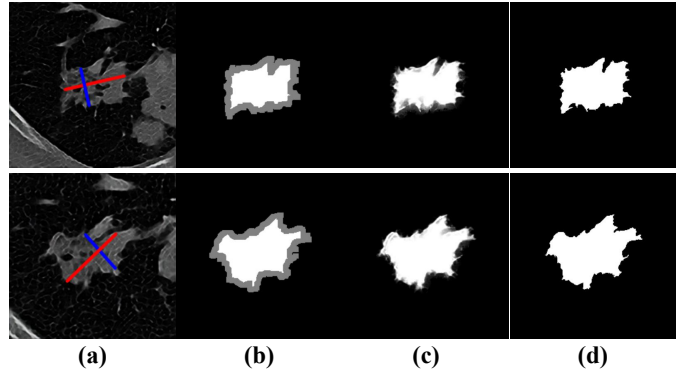


Fig. 2. (a) Lung nodules with RECIST marks. The **red line** is the long axis and the **blue line** is the short axis. (b) Trimaps. **White pixels** mean the lesion region. **Black pixels** mean the background region. **Gray pixels** mean the uncertain region. (c) *Soft Masks*. (d) Binarized *Soft Masks*. The *Soft Mask* preserves edge details of lung nodules effectively.

where α means the extent of belonging to the lung nodules region. Here the close-form-matting algorithm [37] is employed to solve the α matrix, which converts the problem into a closed-form solution through linear assumptions and the labeling pixels. The labeling pixels are the key prior information for solving the above problems and are represented by trimap, which consists of lesion pixels, background pixels, and uncertain area pixels shown in Fig. 2 (b). Therefore, it is important to obtain a high-quality trimap.

2) *Labeling of Soft Mask*: We develop an automatic *Soft Mask* labeling pipeline to deal with priors from different datasets.

First, we initialize these different priors into trimaps composed of lesion region, background region, and the uncertain region as shown in Fig. 2 (b). Specifically, we design the following three strategies for the trimap initialization:

(1) **Trimap Generation with the normal binary mask**: We use morphological operations to process the binary mask. Specifically, The lesion region is obtained by the erosion operation, while the non-lesion background region is obtained by the dilation operation, and the uncertain region is in the middle.

(2) **Trimap Generation with the binary mask of different doctors**: In order to improve the quality and reliability of labeling, some datasets are repeatedly labeled by different doctors. In LIDC dataset [38], the mask for each lung nodule is marked by four different doctors, as shown in Fig. 1 (b). We set the intersection of these different masks labeled by doctors as the lesion region, while we set the complement of the union of these masks to the background region, and other pixels belong to the uncertain region. Formally it can be expressed as:

$$L = M_{d1} \cap M_{d2} \cap M_{d3} \cap M_{d4}, \quad (2)$$

$$B = \overline{M_{d1} \cup M_{d2} \cup M_{d3} \cup M_{d4}}, \quad (3)$$

$$U = \overline{L \cup B}, \quad (4)$$

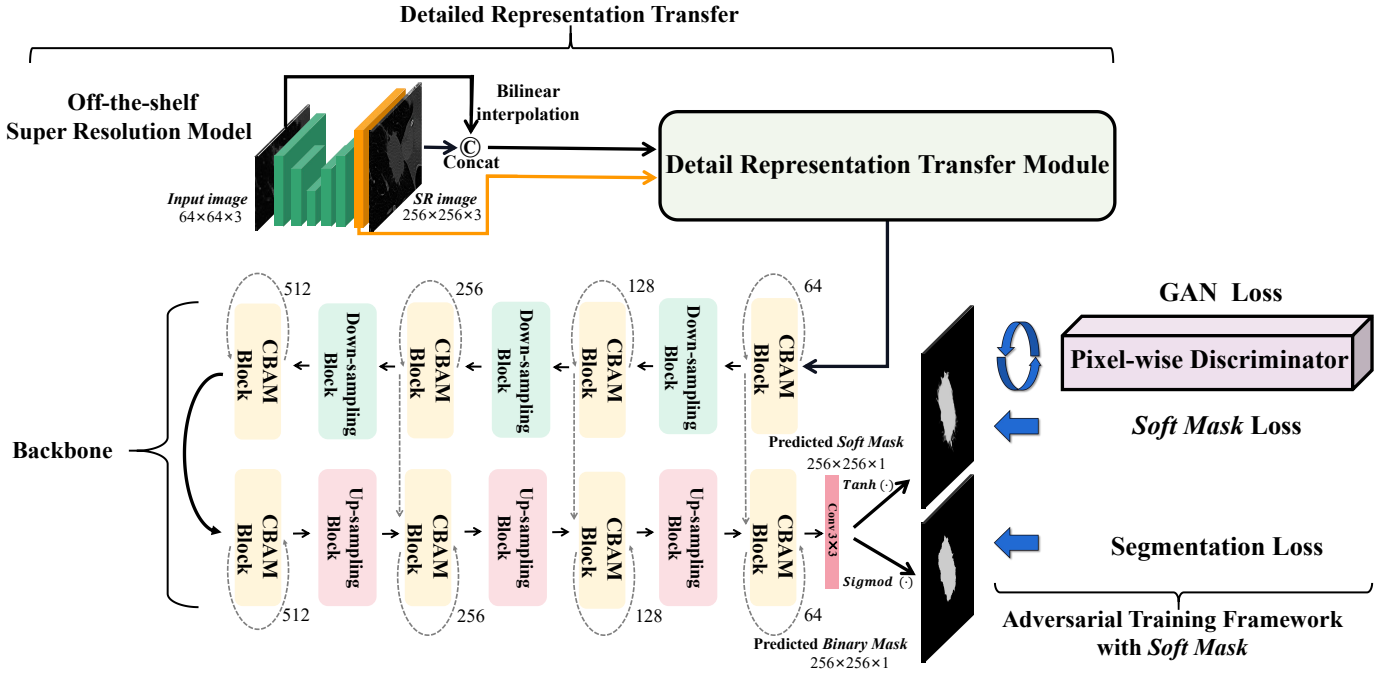


Fig. 3. Overview of the our DSNet. Our DSNet is composed of detail representation transfer module, backbone network and adversarial training framework with *Soft Mask*.

where L denotes lesion region, B denotes background region and U denotes uncertain region, with M_{di} representing the manual annotation of the i -th doctor.

(3) Trimap Generation with RECIST marks: RECIST marks [8] are commonly found in current hospital picture and archiving systems (PACS) despite their coarseness. This means that converting these massive RECIST marks data into accurate masks will have great application value and potential. As shown in Fig. 2 (a), RECIST marks have a long axis and a short axis to mark the diameters of the lesion. First, we use the regions marked on the long axis and the short axis as the prior information of the GrabCut [9] to obtain the initial rough binary masks. Then we apply the morphological processing mentioned in **strategy (1)** to get the trimap.

After obtaining the reliable trimap, we use the close-form-matting algorithm [37] to generate *Soft Masks* shown in Fig. 2 (c). Since solving α for each pixel in Eq. 1 is an ill-posed problem, appropriate conditional assumptions need to be made. The close-form-matting algorithm [37] assumes that the foreground L and background B are almost unchanged in a small window centered on any pixel, i.e. the foreground and background satisfy local smoothness. Base on this assumption, Eq. 1 can be re-expressed as:

$$\alpha_i \approx aM_i + b, \quad \forall i \in w \quad (5)$$

where $a = \frac{1}{L-B}$, $B = -\frac{B}{F-B}$, and w is a small window in image. This approximate expression suggests finding $\alpha, a,$ and b that minimize the cost function as:

$$J(\alpha, a, b) = \sum_{j \in M} \left(\sum_{i \in w_j} (\alpha_i - a_j M_i - b_j)^2 + \epsilon a_j^2 \right) \quad (6)$$

where w_j is a small window around pixel j , and the ϵa_j^2 is a regularization term on a to obtain numerically stable and smooth solutions. For an image with N pixels, there are $3N$ unknowns in Eq. 6. After a series of derivations and proofs [37], the cost function can be simplified to:

$$J(\alpha) = \alpha^T L \alpha, \quad (7)$$

where L is a $N \times N$ matrix, whose (i, j) entry is:

$$\sum_{k|(i,j) \in w_k} \left(\delta_{i,j} - \frac{1}{|w_k|} \left(1 + \frac{1}{\frac{\epsilon}{|w_k|} + \sigma_k^2} (M_i - \mu_k)(M_j - \mu_k) \right) \right). \quad (8)$$

Here, $\delta_{i,j}$ is the Kronecker delta, μ_k and σ_k^2 are the mean and variance of the intensities in the window w_k around k , while $|w_k|$ is the number of pixels in this window. In general, the close-form-matting algorithm constructs a Laplacian weight matrix by assuming the smoothness of the local small window and exploiting the correlation between each pixel in the local small window. Then we take the explicit α given by trimap as a constraint, and the optimal value of the cost function can be obtained by solving the minimum eigenvector of the L weight matrix, so as to obtain the solution of the entire α matrix. Finally, substitute α into Eq. 1 to obtain the *Soft Mask*.

Based on the above automated pipeline, we label the lung nodules in the DeepLesion datasets [39] with RECIST marks to get *Soft Masks*. Then, we further binarize (with 0.5 as the threshold) *Soft Masks* to get an accurate binary mask (Fig. 2 (d)) for the lung nodules segmentation task. Besides, the entire pipeline is efficient, which only takes 20 *ms* (for a single 256×256 image: trimap 5 *ms*, close-form-matting 15 *ms*) for us to obtain a high-quality *Soft Mask* label. We label the lung nodules in the DeepLesion datasets [39] with

RECIST marks and form a new dataset containing 1500 lung nodules named *Soft Mask* dataset of Lung Nodules (*LNSM*).

B. Lung Nodule Segmentation Network with Detailed Representation Transfer and Soft Mask Supervision (DSNet)

Our DSNet can transform low-quality lung nodule images into a high-quality mask for accurate segmentation shown in Fig. 3. Specifically, we first design a Detailed Representation Transfer Module (DRTM) to collect feature maps with detailed representations as the input to the network. Then we employ a special backbone network to extract features and output prediction results.

1) *Backbone Architecture*: Based on the classic encoder-decoder architecture of U-Net [23], we design a special backbone to adapt to the accurate segmentation of lung nodules. As shown in Fig. 3, our backbone consists of basic blocks, up-sampling blocks, and down-sampling blocks. The CBAM block [40] is employed as the basic block of our backbone shown in Fig. 4, which uses both channel attention and spatial attention to enhance the expressive ability of feature maps and thus stimulate the performance of segmentation. In addition, the shortcut connection of ResNet [41] is also utilized to ensure the propagation of detailed information and gradients. In order to reduce the loss of detail caused by down-sampling on the input image whose resolution is usually low, we use 4×4 convolution layer with *stride* = 2, *padding* = 1 and ReLU activation function as the down-sampling block instead of pooling. The up-sampling block of the decoder consists of 4×4 transposed convolution and ReLU activation function, while the skip connection of U-Net is still retained to recover the detailed information.

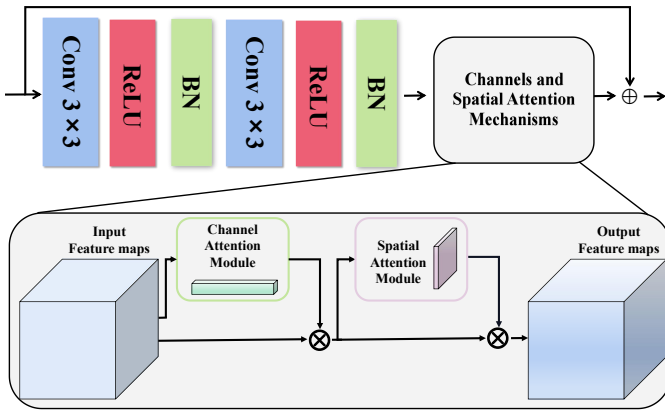


Fig. 4. Details of the CBAM Block in Fig. 3. Each 3×3 convolutional layer is followed by a ReLU activation function and a batch normalization layer.

2) *Segmentation Head*: After a 3×3 convolutional layer, the predicted segmentation mask is generated and accepts the joint supervision of the binary mask (after *Sigmoid*) and the *Soft Mask* (after *Tanh* which normalizes the result to $[-1,1]$). We also normalize the ground truth of *Soft Mask* to the same range via the normalization function in Pytorch [42].

3) *Detailed Representation Transfer*: Lung nodules are usually very small ($5 \sim 10$ mm), so common CT systems can only obtain images of lung nodules with low resolution. The

low-resolution image means the loss of detailed information, which is challenging for accurate segmentation of lung nodules with complex shapes and blurred edges. Inspired by super-resolution methods, we reconstruct the detailed information in the high-resolution image and use it to stimulate the performance of accurate segmentation. Next we will show how to train a super-resolution model without high-resolution lung nodules data and apply the detailed information from the off-the-shelf super-resolution model to the segmentation pipeline. (1) **Self-supervised super-resolution model**: The lack of high-resolution lung nodules images makes it difficult to train a super-resolution model. Due to the robustness of the super-resolution methods [16] and the inspiration of the self-supervised pre-training methods [15], we self-supervised train a super-resolution module with a general CT images dataset DeepLesion [39]. The DeepLesion dataset consists of 32,735 important clinical radiological findings (lesions, tumors, lymph nodes, etc.), and it can be universally adapted to the data of different organs. Specifically, we down-sample the CT images of the Deeplesion dataset from 512×512 to 128×128 for training an SRGAN model [16] (from 128 to 512). Then the trained off-the-shelf super-resolution model is used as a teacher model to transfer the learned detailed knowledge to the Detailed Representation Transfer Module (DRTM) for further lung nodules segmentation.

For transferring the detailed representation into the segmentation pipeline, we designed our DRTM to capture detailed representations as follows.

(2) **Detailed Representation Transfer Module**: First, our DRTM uses the context branch and the detail branch to extract feature maps respectively, as shown in Fig. 5. For the context branch, we combine the interpolated low-resolution image and the output of the SR model and use the convolutional layer to extract the feature maps \mathcal{F}_c . For the detail branch, we explicitly mine detail representations from the feature map output of the last block of the SR model decoder. Specifically, given the input feature maps from SR model $\mathcal{F}_{SR} \in \mathbb{R}^{H \times W \times C}$, we use two groups of convolutions to extract features from different receptive fields. We explicitly model high-frequency detail information by subtracting the outputs of these two convolutional layers as follows:

$$\mathcal{F}_h = \text{sigmoid}(C_h(\mathcal{F}_{SR}) - C_l(\mathcal{F}_{SR})), \quad (9)$$

where C_h denotes 1×1 point-wise convolution and C_l denotes 3×3 dilated convolution with dilated rate 2. Here we use point-wise convolution C_h to preserve local high-frequency details, and employ dilated convolution C_l with a large receptive field to extract low-frequency semantic structure information. Therefore, the high-contrast pixels obtained by their subtraction are regarded as high-frequency detail information. Then \mathcal{F}_h is utilized to weight the original feature map to achieve the detailed texture enhancement as:

$$\mathcal{F}_d = \mathcal{F}_{SR} \times \mathcal{F}_h, \quad (10)$$

where \mathcal{F}_d is the feature maps output by the detail branch.

However, not all detailed representations from the super-resolution model are conducive to the segmentation, and some noises also are introduced shown in Fig. 6 (b). To suppress

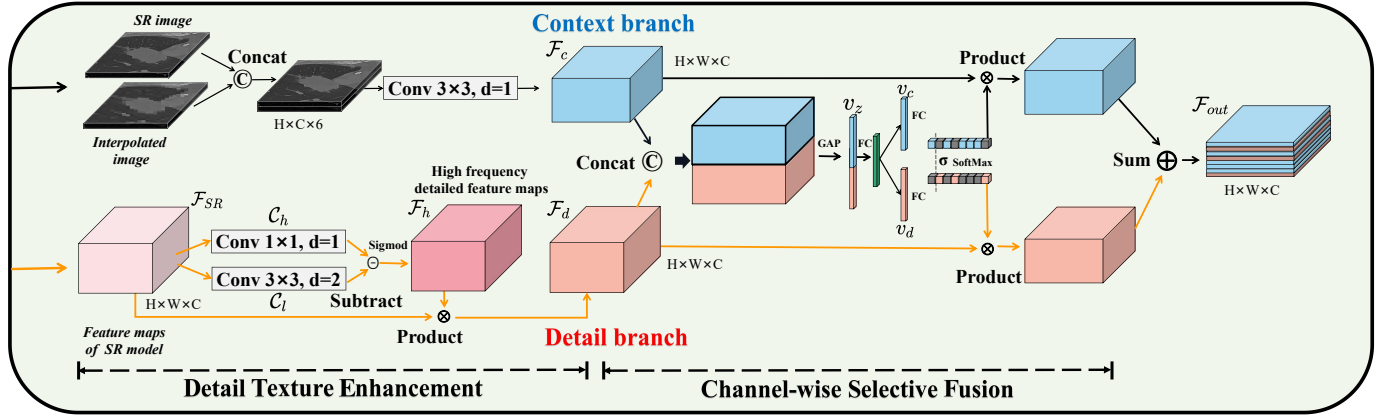


Fig. 5. Detailed design of Detailed Representation Transfer Module (DRTM). Our DRTM includes two operations, detail texture enhancement and channel-selective fusion, to adaptively capture detailed representations from super-resolution (SR) models.

the noise and better fusion the detailed representation, we further propose a novel channel-wise selective fusion operation. Specifically, two compact vectors $v_c, v_d \in \mathbb{R}^{1 \times C}$ are created to enable the guidance for the precise and adaptive selections. This is achieved by the simple Global Average Pooling (GAP) and fully connected (FC) layer:

$$v_z = \text{GAP}(\text{Concat}(\mathcal{F}_d, \mathcal{F}_c)), \quad (11)$$

where Concat denotes merging two feature maps along the channels. Then we use GAP to generate vector $v_z \in \mathbb{R}^{1 \times 2C}$.

$$v_c, v_d = \text{FC}(v_z), \quad (12)$$

Here the fully connected layer (FC) reduces v_z to $\mathbb{R}^{1 \times C}$ dimension and then predicts two weight vectors v_c, v_d for the two branches respectively.

Then, a soft attention across channels is used to select different spatial scales of information adaptively, which is guided by the compact vectors v_c, v_d . Specifically, a softmax operator is applied on the channel-wise digits:

$$a = \frac{e^{v_c}}{e^{v_c} + e^{v_d}}, b = \frac{e^{v_d}}{e^{v_c} + e^{v_d}} \quad (13)$$

where $a, b \in \mathbb{R}^{1 \times C}$ denote the soft attention vectors for \mathcal{F}_c and \mathcal{F}_d , respectively. The final output feature maps $\mathcal{F}_{out} \in \mathbb{R}^{H \times W \times C}$ is obtained through the weighted fusion:

$$\mathcal{F}_{out} = a \cdot \mathcal{F}_c + b \cdot \mathcal{F}_d, \quad a + b = 1 \quad (14)$$

In addition, Fig. 6 (c) and (d) show the spatial attention maps in the first CBAM block of DSNet. Here sample (c) is to directly use the feature maps \mathcal{F}_{SR} of the super-resolution model as input while sample (d) is to use DRTM for representation transfer. We can see more impressive edge details (thanks to detail texture enhancement) and less sharpening noises (thanks to channel-wise selective fusion) with the help of our DRTM.

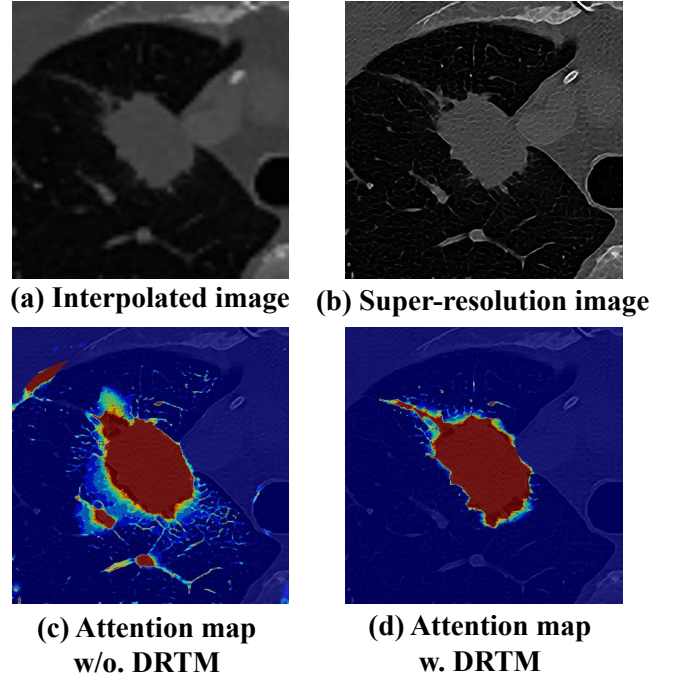


Fig. 6. Some visualization samples. DRTM: Detailed Representation Transfer Module.

C. Adversarial training framework with Soft Mask.

We use DICE loss [43] as the **Segmentation Loss** for the supervision of ground truth binary masks:

$$\mathcal{L}_{\text{Seg}} = 1 - \frac{2 \sum_{i=1}^N (x_i y_i)}{\sum_{i=1}^N x_i^2 + \sum_{i=1}^N y_i^2}. \quad (15)$$

where y_i is the ground truth segmentation mask Y_{bin} for a given pixel i , and x_i is the corresponding value in the predicted binary mask X_{bin} .

Soft Mask Loss is given to make the predicted *Soft Mask* has the same distribution as the ground truth *Soft Mask*:

$$\mathcal{L}_{\text{Soft}} = \|X_{\text{soft}} - Y_{\text{soft}}\|_{L1} \quad (16)$$

Where X_{soft} and Y_{soft} denote ground truth *Soft Mask* and predicted *Soft Mask* respectively, and $\|\cdot\|_{L1}$ denotes the $L1$ distance.

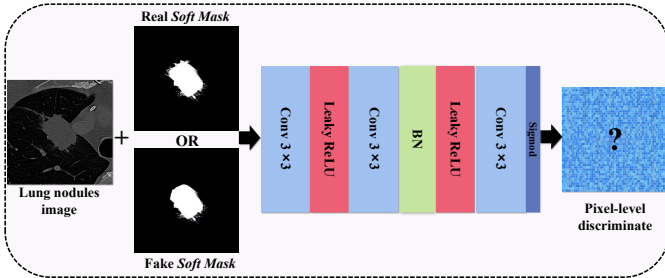


Fig. 7. The structure of the pixel-wise Discriminator.

GAN Loss is introduced to further improve the quality of the predicted *Soft Mask* by conditional generative adversarial supervision [44]. As shown in Fig 7, a pixel-wise Discriminator is designed to provide adversarial GAN loss for DSNet. Notice that pixel-level discrimination is utilized to obtain an accurate pixel-wise adversarial loss. Specifically, the overall objective can be expressed as:

$$G^* = \arg \min_S \max_D \mathcal{L}_{GAN}(S, D), \quad (17)$$

$$\mathcal{L}_{GAN} = \log D(x, y) + \log(1 - D(x, S(x))) \quad (18)$$

where our DSNet S tries to minimize this objective against an adversarial Discriminator D that tries to maximize it. The x denotes the lung nodules image (condition), y denotes the real *Soft Mask* (ground truth), and $S(x)$ denotes the fake *Soft Mask* (predicted *Soft Mask*). In the training framework, our DSNet and the Discriminator have trained alternately.

D. Implementation

The total loss function of our DSNet can be defined as :

$$\mathcal{L}_{total} = \lambda_1 \mathcal{L}_{Seg} + \lambda_2 \mathcal{L}_{Soft} + \lambda_3 \mathcal{L}_{GAN} \quad (19)$$

where $\lambda_1, \lambda_2, \lambda_3$ are empirically set to 0.5, 100, 1. The Adam optimizer [45] with poly learning rate policy is used to optimize the network with the training batch size set to 4. The learning rate decays from $2e^{-4}$, and the whole training process for all datasets typically converges in about 100 epochs with a single NVIDIA Titan V GPU.

IV. EXPERIMENTS

A. Accurate segmentation for lung nodules

In this section, we have conducted comprehensive experiments on the proposed *LNSM* and LIDC [38] datasets to verify the effectiveness of our method on lung nodules segmentation. Following previous works [11] and [14], DICE similarity (DICE), sensitivity (SEN) and positive predictive value (PPV) are used as the evaluation metrics. Here DICE score is a region-level similarity measure that mainly focuses on the internal structural consistency of segmented objects, while

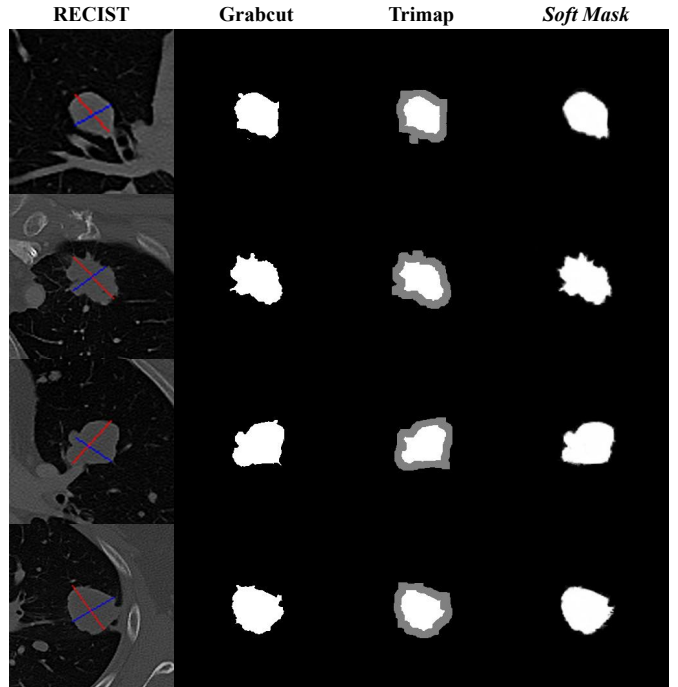


Fig. 8. Examples of *Soft Mask* annotation pipeline of LNSM dataset.

SEN and PPV are pixel-level evaluation measures that equally consider the influence of each pixel to give the error value between the predicted mask and the ground truth. For convenient, we use the following denotations: TP (true positive), TN (true negative), FP (false positive), and FN (false negative). Therefore, these metrics are correspondingly defined as:

$$DICE = \frac{2 \times TP}{2 \times TP + FP + FN}, \quad (20)$$

$$SEN = \frac{TP}{TP + FN}, \quad (21)$$

$$PPV = \frac{TP}{TP + FP}. \quad (22)$$

1) *Comparison on our LNSM dataset:* Lung nodule images with RECIST marks in Deeplesion dataset [39] are used to build our *LNSM* dataset. According to the method (**strategy (3)**) in Sec. III-A1) proposed in the previous section, we obtained 1500 cropped 64×64 lung nodules images with *Soft Masks* and binary masks for training supervision. We show in Fig. 8 the steps to automatically obtain the *Soft Mask* via the RECIST marks. We randomly divide the dataset into training sets (1,000 nodules), test sets (400 nodules), and validation sets (100 nodules), while all methods use the same dataset division. In the test, all methods utilize the same binary mask in *LNSM* as the ground truth to calculate metrics for a fair comparison.

Table I presents a quantitative comparison of some advanced methods on *LNSM* dataset with the same dataset settings. The outputs are in “mean \pm standard deviation” format. Specifically, UNet [23], CF-CNN [11], DB-ResNet [14],

TABLE I
EVALUATION RESULTS ON OUR *LNSM* DATASET.

Methods	DICE (%)	SEN (%)	PPV (%)
UNet [23]	87.88 ± 1.1	86.62 ± 3.2	89.04 ± 5.7
CF-CNN [11]	88.98 ± 2.5	87.20 ± 3.2	89.60 ± 2.3
DB-ResNet [14]	89.21 ± 2.2	88.22 ± 1.6	90.04 ± 1.8
UNet++ [24]	88.57 ± 2.7	89.24 ± 0.5	91.86 ± 3.7
INFNet [25]	90.05 ± 1.8	88.17 ± 2.3	93.41 ± 3.7
INFNet [†] [25]	90.53 ± 1.7	89.21 ± 1.3	94.04 ± 2.5
MedT [28]	90.13 ± 2.6	89.56 ± 3.1	92.41 ± 1.2
MedT [†] [28]	91.02 ± 2.4	90.10 ± 1.5	93.12 ± 2.7
DSNet (our)	93.77 ± 3.1	91.76 ± 0.9	95.88 ± 2.5

UNet++ [24], INFNet [25], and recent MedT [28] are compared. Here [†] represents using SR image output by super-resolution model we got in Sec. III-B3 (1) as the input. We can see that our DSNet exceeds these state-of-the-art methods with a large margin, especially on the DICE and PPV metric scores.

2) *Comparison on LIDC*: We used a public lung nodules CT dataset from the Lung Image Database Consortium and Image Database Resource Initiative (LIDC) [38] for further comparison. In this study, we studied 986 nodule samples annotated by four radiologists. Due to the differences in labeling between the four radiologists, the 50 % consensus criterion [46] was used to generate the ground truth binary masks. We use the method (**strategy(2) in Sec. III-A1**) of labeling *Soft Mask* to obtain ground truth *Soft Masks* for training supervision. Then, we randomly partition these nodules into three subsets for training, validation, and testing with the number of nodules contained in each subset being 387, 55, and 544, respectively.

We compared our DSNet with some advanced segmentation methods including UNet [23], CF-CNN [11], DB-ResNet [14], UNet++ [24], INFNet [25], and MedT [28], which are illustrated in Tab. II. Noted that [†] represents using SR image output by super-resolution model we got in Sec. III-B3 (1) as the input. The results show that our method outperforms other methods in all metrics. Compared with the most competitive MedT[†], our method leads 2.81%, 2.23%, and 3.68% respectively. Besides, the visual comparison between our DSNet and these methods on the LIDC dataset is shown in Fig. 9.

B. Ablation study

To validate the effectiveness of our modules and strategies, we conduct the following ablation studies on both *LNSM* and LIDC datasets.

1) *Comprehensive Ablation Study*: The ablation study is reported in Tab. III. We use the classic UNet [23] trained with DICE loss as the baseline. After replacing with our backbone, the performance is significantly improved, which implies that the network structure is still crucial to lung nodules segmentation. Just using super-resolution images as the input, the DICE score has also been slightly improved, indicating that

TABLE II
EVALUATION RESULTS ON THE LIDC DATASET.

Methods	DICE (%)	SEN (%)	PPV (%)
UNet [23]	77.84 ± 21.7	77.98 ± 24.5	82.52 ± 21.5
CF-CNN [11]	78.55 ± 12.5	86.01 ± 15.2	75.79 ± 14.7
DB-ResNet [14]	82.74 ± 10.2	89.05 ± 11.8	79.64 ± 13.5
UNet++ [24]	80.54 ± 12.9	87.96 ± 17.2	79.18 ± 15.1
INFNet [25]	81.01 ± 14.1	88.33 ± 13.7	75.58 ± 17.6
INFNet [†] [25]	81.67 ± 13.7	87.25 ± 10.5	76.24 ± 13.3
MedT [28]	81.34 ± 7.9	87.96 ± 11.4	80.14 ± 15.3
MedT [†] [28]	82.08 ± 6.5	88.33 ± 11.8	81.01 ± 16.4
DSNet (our)	84.89 ± 7.2	90.56 ± 12.0	84.69 ± 13.4

TABLE III
ABLATION STUDY ON THE *LNSM* AND LIDC BENCHMARKS. WE REPORT THE *DICE* SCORES FOR DIFFERENT VARIANTS OF OUR DSNET.

Method		<i>LNSM</i>	LIDC
<i>Config.</i>	<i>Variants</i>	<i>DICE (%)</i>	<i>DICE (%)</i>
Backbone (Baseline)	<i>orig. UNet</i>	87.88 ± 1.1	77.84 ± 21.7
	our proposed backbone	89.57 ± 1.3	79.3 ± 25.3
+ Representation Transfer	+ SR Input + DRTM	90.15 ± 2.1 91.83 ± 1.7	81.69 ± 15.7 83.88 ± 8.5
+ Adversarial training with <i>Soft Mask</i>	+ <i>Soft Mask</i> Loss + GAN Loss (our DSNet)	93.26 ± 2.0 93.77 ± 3.1	84.21 ± 10.3 84.89 ± 7.2

high-resolution images can promote the accurate segmentation of lung nodules. Note that our DRTM further improves the performance indicating the importance of detail texture enhancement and channel-wise selective fusion. Finally, our DSNet achieves the best performance after applying complete adversarial training with *Soft Mask* supervision.

TABLE IV
COMPARISON OF DIFFERENT SOFT LABELS.

Soft Labels	LNSM DICE(%)	LIDC DICE(%)
w/o. soft label supervision	91.23 ± 1.7	82.88 ± 8.5
Soft label in [30]	91.92 ± 2.5	83.11 ± 8.6
Soft label in [31]	92.66 ± 1.4	83.95 ± 10.3
Our <i>Soft Mask</i>	93.77 ± 3.1	84.89 ± 7.2

2) *Ablation Study on Soft Mask Supervision*: In addition, Tab. IV reports the comparison between our *Soft Mask* and other soft labels [30], [31]. Specifically, we use them to supervise the training of our DSNet under the same conditions, respectively. The results demonstrate that our *Soft Mask* is significantly better than other soft labels, due to the more

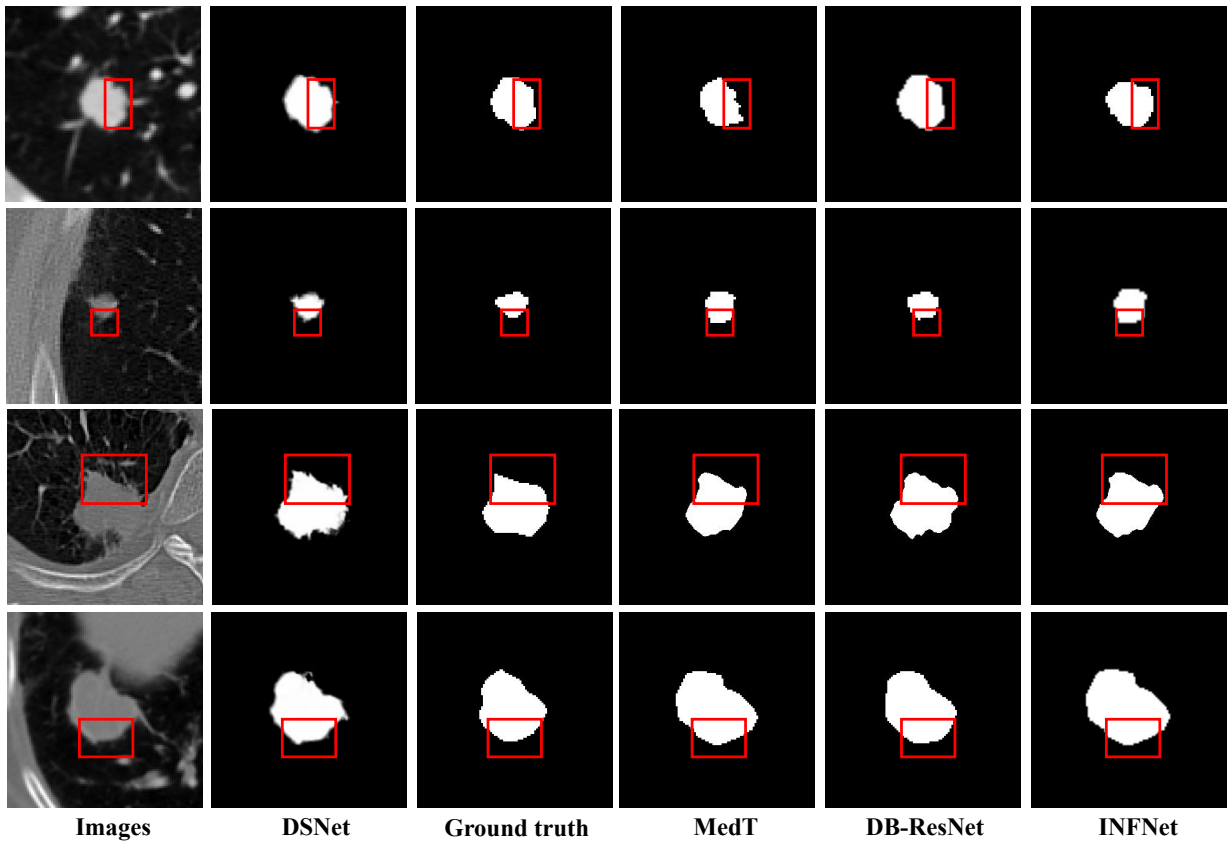


Fig. 9. Visual comparison between our DSNet and advanced methods on LIDC [38] dataset. Thanks to the *Soft Mask* supervision, our DSNet has an impressive visual effects that even exceeds binary ground truth.

TABLE V
ABLATION STUDY ON OUR DRTM. DTM: DETAIL TEXTURE ENHANCEMENT; CSF: CHANNEL-WISE SELECTIVE FUSION.

Operations		LNSM	LIDC
DTM	CSF	DICE(%)	DICE(%)
		92.62 ± 1.5	83.64 ± 8.4
✓		93.41 ± 1.2	84.26 ± 7.5
✓	✓	93.77 ± 3.1	84.89 ± 7.2

accurate edge representation of our *Soft Mask* which reduces the impact of imprecise boundary annotation.

3) *Ablation Study on Detail Representation Transfer*: We also perform a meticulous ablation study for each component in our DRTM, as shown in Tab. V. The results show that the optimal DICE score is achieved when both operations detail texture enhancement and channel-wise selective fusion are applied.

C. Robustness Study

To further verify the accurate segmentation performance and generalization of our method, we design an ambitious and challenging experiment: compare our DSNet with human doctors. Specifically, we compare our DSNet trained on *LNSM* dataset with four radiologists on LIDC. Note that our DSNet

is not retrained, which means that the training set and the test set are cross-domain.

TABLE VI
COMPARE OUR DSNET WITH FOUR HUMAN DOCTORS ON LIDC DATASET. D1, D2, D3, D4 MEAN DOCTOR 1, DOCTOR 2, DOCTOR 3, DOCTOR 4 RESPECTIVELY.

DICE (%)	D1	D2	D3	D4	50% Consensus	DSNet
D1	-	70.65	73.14	62.57	77.51	77.76
D2	70.65	-	74.46	64.91	82.92	74.30
D3	73.14	74.46	-	76.31	83.01	80.88
D4	62.57	64.91	76.31	-	69.74	69.71
50% Consensus	77.51	82.92	83.01	69.74	-	86.35
DSNet	77.76	74.30	80.88	69.71	86.35	-

Tab. VI shows the comparison results of our DSNet and four human doctors on the LIDC dataset. The DICE between any two masks (row and column) is reported in the table. Due to the differences and contradictions in labeling between the four radiologists, the 50 % consensus criterion [46] is often used as the ground truth. It can be observed from Tab. VI that our DSNet, even though it is trained on *LNSM* dataset, is still closer to 50% consensus than all doctors. On the one hand,

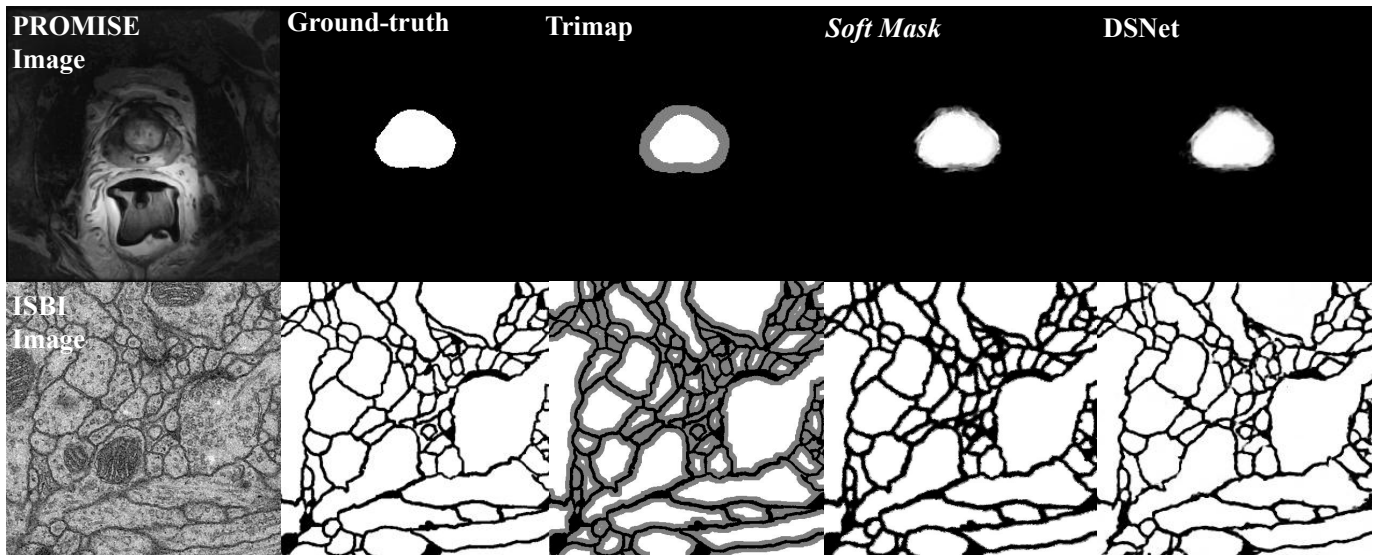


Fig. 10. Some visual results on ISBI and PROMISE. From left to right are the original image, the ground truth binary mask of the dataset, the trimap image (Obtained by labeling strategy (1)), and the *Soft Mask* and the results of our DSNet prediction.

the results demonstrate that our DSNet has strong robustness and can deal with cross-domain challenges, which implies the potential for clinical application. On the other hand, the results mean that the *LNSM* dataset we proposed is also universal and robust. In addition, Fig. 11 shows the visual comparison results between our DSNet and doctors. Our DSNet not only has a higher DICE score but also has an impressive visual result that even exceeds ground truth (50 % Consensus). It’s worth mentioning that our visual results also have been approved by clinical experts.

while PROMISE consists of three subsets: training, verification, and testing ((460, 65, and 130 samples respectively). We use the *Soft Mask* labeling **strategy (1)** proposed in Sec. III-A1 to obtain the *Soft Masks* for supervision. As shown in Tab. VII, Our DSNet achieves the highest DICE and PPV scores and competitive SEN scores on these tasks that also require accurate segmentation. Our DSNet is also competent for medical segmentation tasks from cells (ISBI) to organs (PROMISE) and shows excellent generalization.

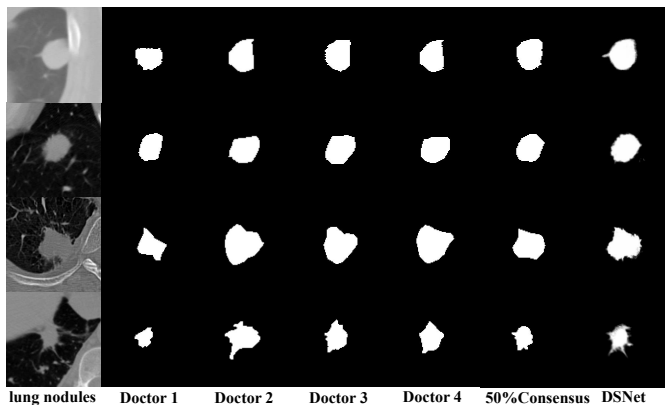


Fig. 11. Visual comparison results between our DSNet and doctors. **Our DSNet has an amazing visual effects that even exceeds binary ground truth (50 % consensus).**

D. Generalization Study

To verify the generalization of our method to other medical tasks, we perform experiments on ISBI [47] and PROMISE [48]. The ISBI is a neuronal structure segmentation dataset and the PROMISE is a prostate MRI dataset. After data augmentation, ISBI consists of three subsets: training, verification, and testing (210, 60, and 30 samples respectively),

TABLE VII
COMPARISON OF METHODS ON ISBI AND PROMISE. THE **LEFT** COLUMN: RESULTS OF ISBI. THE **RIGHT** COLUMN: RESULTS OF PROMISE.

Methods	UNet	UNet3+	INFNet	MedT	DSNet
DICE (%)	93.5 87.9	94.3 91.5	94.5 90.0	93.7 91.4	95.9 92.3
SEN (%)	91.4 88.7	89.9 87.8	92.1 88.6	90.7 89.0	90.8 88.6
PPV (%)	91.3 90.4	94.1 93.3	94.3 92.3	94.4 93.1	94.8 93.5

E. Discussions

1) *Time Consumption*: One limitation of our method is that our method may introduce additional time consumption. On the one hand, the training phase requires additional time consumption when constructing the *Soft Mask* supervision. However, our annotation pipeline is automatic and efficient as reported in Sec. III-A2. Our method only takes 20 *ms* (trimap 5 *ms*, close-form-matting 15 *ms*) for a 256×256 image to obtain a high-quality *Soft Mask* label. Once the *Soft Mask* dataset is obtained, this part of the time consumption will no longer be burdened. Besides, the discriminator is deprecated during the inference phase without increasing computational cost. On the other hand, our Detailed Representation Transfer causes computational cost due to the super-resolution model. But note that the detail representation transfer is designed to

deal with low-resolution segmentation tasks, while the input size of the super-resolution model is small, so the operating efficiency of the overall pipeline will not be significantly affected. Compared with the performance improvement, this extra calculation is worthy.

TABLE VIII
INFERENCE TIME ABLATION ON LNSM DATASET. DRF: DETAILED REPRESENTATION TRANSFER.

Config.	LNSM	LIDC	Inference time (ms)
	DICE(%)	DICE(%)	
w/o. DRF (SoftGAN [17])	91.63 ± 3.2	83.21 ± 7.0	5.1
w. DRF	93.77 ± 3.1	84.89 ± 7.2	6.7

Tab. VIII shows our speed test results on the LNSM dataset. The speed is averaged on images (64×64) with a single NVIDIA Titan V GPU. In the future, we will explore the use of lighter super-resolution networks [49], knowledge distillation [50], and pre-trained models [51] to further reduce the computational cost of detail representation transfer.

2) *Relationship with Label Smooth*: Our *Soft Mask* labeling can also be seen as a regularization strategy that softens the traditional one-hot type of label like label smooth in knowledge distillation [52], [53], which can effectively suppress the over-fitting when calculating loss values. Specifically, using an independent distribution $u(y)$, the original ground truth distribution $q(y|x)$ and $u(y)$ are mixed and mapped to $q'(y|x)$:

$$q'(y|x) = (1 - \epsilon) * q(y|x) + \epsilon u(y) \quad (23)$$

which is consistent with our practice by using the *Soft Mask* as the ground truth for training. The *Soft Mask* softens the binary labels, alleviating sample imbalance and overfitting during training. Besides, the non-binary labels of edge regions contain richer structural information like teacher model output in the knowledge distillation.

3) *Relationship with Prompt Learning in NLP*: Our *Soft Mask* supervision is similar to the prompt learning [54] that has attracted widespread attention in the natural language processing (NLP) field recently. It can be considered that the learning of the main task (lung nodules segmentation) is improved by adding a promotion task (*Soft Mask* generation). Therefore, our method can be regarded as an innovative attempt to prompt learning in the fields of computer vision and medical image processing.

4) *Relationship with Traditional Image Processing Algorithms*: Deep learning algorithms based on neural networks have become popular in medical image processing, but traditional image processing algorithms can still bring good inspiration. In this work, we use some traditional image processing techniques and ideas including: close-form-matting [37], Grab-Cut [9], morphological processing [55], and high frequency decomposition [56]. We explore and validate the possibility and potential of incorporating these traditional algorithms in a deep learning-based segmentation framework.

V. CONCLUSION

In this work, we propose a complete solution for accurate lung nodule segmentation, including the *Soft Mask* labeling

pipeline and a novel DSNet, which not only improves the network structure but also the quality of the input image and ground truth. Our method is validated to be robust and universally effective on both lung nodule segmentation and other medical datasets, and has great potential to segment other small lesions or small objects accurately while obtaining impressive visual results.

VI. ACKNOWLEDGMENT

We sincerely thank the reviewers and associate editors for their helpful comments and suggestions on improving this article.

REFERENCES

- [1] C. Wang, P. W. Horby, F. G. Hayden, and G. F. Gao, "A novel coronavirus outbreak of global health concern," *The lancet*, vol. 395, no. 10223, pp. 470–473, 2020.
- [2] R. Wang, C. Ji, Y. Zhang, and Y. Li, "Focus, fusion, and rectify: Context-aware learning for covid-19 lung infection segmentation," *IEEE Transactions on Neural Networks and Learning Systems*, vol. 33, no. 1, pp. 12–24, 2021.
- [3] R. L. Siegel, K. D. Miller, and A. Jemal, "Cancer statistics, 2019," *CA: a cancer journal for clinicians*, vol. 69, no. 1, pp. 7–34, 2019.
- [4] H. MacMahon, J. H. Austin, G. Gamsu, C. J. Herold, J. R. Jett, D. P. Naidich, E. F. Patz Jr, and S. J. Swensen, "Guidelines for management of small pulmonary nodules detected on ct scans: a statement from the fleischner society," *Radiology*, vol. 237, no. 2, pp. 395–400, 2005.
- [5] F. Liao, M. Liang, Z. Li, X. Hu, and S. Song, "Evaluate the malignancy of pulmonary nodules using the 3-d deep leaky noisy-or network," *IEEE transactions on neural networks and learning systems*, vol. 30, no. 11, pp. 3484–3495, 2019.
- [6] J. Pedrosa, G. Aresta, C. Ferreira, M. Rodrigues, P. Leitão, A. S. Carvalho, J. Rebelo, E. Negrão, I. Ramos, A. Cunha *et al.*, "Lndb: a lung nodule database on computed tomography," *arXiv preprint arXiv:1911.08434*, 2019.
- [7] J. Cai, Y. Tang, L. Lu, A. P. Harrison, K. Yan, J. Xiao, L. Yang, and R. M. Summers, "Accurate weakly supervised deep lesion segmentation on ct scans: Self-paced 3d mask generation from recist," *arXiv preprint arXiv:1801.08614*, 2018.
- [8] E. A. Eisenhauer, P. Therasse, J. Bogaerts, L. H. Schwartz, D. Sargent, R. Ford, J. Dancy, S. Arbuck, S. Gwyther, M. Mooney *et al.*, "New response evaluation criteria in solid tumours: revised recist guideline (version 1.1)," *European journal of cancer*, vol. 45, no. 2, pp. 228–247, 2009.
- [9] C. Rother, V. Kolmogorov, and A. Blake, "'grabcut" interactive foreground extraction using iterated graph cuts," *ACM transactions on graphics (TOG)*, vol. 23, no. 3, pp. 309–314, 2004.
- [10] B. Lassen, C. Jacobs, J. Kuhnigk, B. Van Ginneken, and E. Van Rikxoort, "Robust semi-automatic segmentation of pulmonary subsolid nodules in chest computed tomography scans," *Physics in Medicine & Biology*, vol. 60, no. 3, p. 1307, 2015.
- [11] S. Wang, M. Zhou, Z. Liu, Z. Liu, D. Gu, Y. Zang, D. Dong, O. Gevaert, and J. Tian, "Central focused convolutional neural networks: Developing a data-driven model for lung nodule segmentation," *Medical image analysis*, vol. 40, pp. 172–183, 2017.
- [12] W. Sun, B. Zheng, and W. Qian, "Automatic feature learning using multichannel roi based on deep structured algorithms for computerized lung cancer diagnosis," *Computers in Biology and Medicine*, p. 530, 2017.
- [13] H. Liu, H. Cao, E. Song, G. Ma, and C. C. Hung, "A cascaded dual-pathway residual network for lung nodule segmentation in ct images," *Physica Medica*, vol. 63, pp. 112–121, 2019.
- [14] H. Cao, H. Liu, E. Song, C.-C. Hung, G. Ma, X. Xu, R. Jin, and J. Lu, "Dual-branch residual network for lung nodule segmentation," *Applied Soft Computing*, vol. 86, p. 105934, 2020. [Online]. Available: <https://www.sciencedirect.com/science/article/pii/S156849461930715X>
- [15] K. He, H. Fan, Y. Wu, S. Xie, and R. Girshick, "Momentum contrast for unsupervised visual representation learning," in *2020 IEEE/CVF Conference on Computer Vision and Pattern Recognition (CVPR)*, 2020.

- [16] C. Ledig, L. Theis, Huszar, J. Caballero, A. Cunningham, A. Acosta, A. Aitken, A. Tejani, J. Totz, and Z. Wang, "Photo-realistic single image super-resolution using a generative adversarial network," in *IEEE Computer Society*, 2016.
- [17] C. Wang, R. Xu, S. Xu, W. Meng, J. Xiao, Q. Peng, and X. Zhang, "Softgan: Towards accurate lung nodule segmentation via soft mask supervision," in *IEEE International Conference on Multimedia and Expo (ICME)*, 2022.
- [18] W. J. Kostis, A. P. Reeves, D. F. Yankelevitz, and C. I. Henschke, "Three-dimensional segmentation and growth-rate estimation of small pulmonary nodules in helical ct images," *IEEE transactions on medical imaging*, vol. 22, no. 10, pp. 1259–1274, 2003.
- [19] T. Kubota, A. K. Jerebko, M. Dewan, M. Salganicoff, and A. Krishnan, "Segmentation of pulmonary nodules of various densities with morphological approaches and convexity models," *Medical Image Analysis*, vol. 15, no. 1, pp. 133–154, 2011.
- [20] T. F. Chan and L. A. Vese, "Active contours without edges," *IEEE Transactions on image processing*, vol. 10, no. 2, pp. 266–277, 2001.
- [21] Y. Boykov and V. Kolmogorov, "An experimental comparison of min-cut/max-flow algorithms for energy minimization in vision," *IEEE transactions on pattern analysis and machine intelligence*, vol. 26, no. 9, pp. 1124–1137, 2004.
- [22] D. Wu, L. Lu, J. Bi, Y. Shinagawa, K. Boyer, A. Krishnan, and M. Salganicoff, "Stratified learning of local anatomical context for lung nodules in ct images," in *2010 IEEE Computer Society Conference on Computer Vision and Pattern Recognition*. IEEE, 2010, pp. 2791–2798.
- [23] O. Ronneberger, P. Fischer, T. Brox, , and and, "U-net: Convolutional networks for biomedical image segmentation," in *International Conference on Medical image computing and computer-assisted intervention*. Springer, 2015, pp. 234–241.
- [24] Z. Zhou, M. M. R. Siddiquee, N. Tajbakhsh, and J. Liang, "Unet++: A nested u-net architecture for medical image segmentation," *CoRR*, vol. abs/1807.10165, 2018.
- [25] D.-P. Fan, T. Zhou, G.-P. Ji, Y. Zhou, G. Chen, H. Fu, J. Shen, and L. Shao, "Inf-net: Automatic covid-19 lung infection segmentation from ct images," *IEEE Transactions on Medical Imaging*, vol. 39, no. 8, pp. 2626–2637, 2020.
- [26] N. K. Tomar, D. Jha, M. A. Riegler, H. D. Johansen, D. Johansen, J. Rittscher, P. Halvorsen, and S. Ali, "Fanet: A feedback attention network for improved biomedical image segmentation," *IEEE Transactions on Neural Networks and Learning Systems*, 2022.
- [27] N. Paluru, A. Dayal, H. B. Jensen, T. Sakinis, L. R. Cenkeramaddi, J. Prakash, and P. K. Yalavarthy, "Anam-net: Anamorphic depth embedding-based lightweight cnn for segmentation of anomalies in covid-19 chest ct images," *IEEE Transactions on Neural Networks and Learning Systems*, vol. 32, no. 3, pp. 932–946, 2021.
- [28] J. M. J. Valanarasu, P. Oza, I. Hacihaliloglu, and V. M. Patel, "Medical transformer: Gated axial-attention for medical image segmentation," *arXiv preprint arXiv:2102.10662*, 2021.
- [29] J. Chen, Y. Lu, Q. Yu, X. Luo, E. Adeli, Y. Wang, L. Lu, A. L. Yuille, and Y. Zhou, "Transunet: Transformers make strong encoders for medical image segmentation," *arXiv preprint arXiv:2102.04306*, 2021.
- [30] E. Kats, J. Goldberger, H. Greenspan, , and and, "Soft labeling by distilling anatomical knowledge for improved ms lesion segmentation," in *2019 IEEE 16th International Symposium on Biomedical Imaging (ISBI 2019)*. IEEE, 2019, pp. 1563–1566.
- [31] C. Gros, A. Lemay, and J. Cohen-Adad, "Softseg: Advantages of soft versus binary training for image segmentation," *Medical Image Analysis*, vol. 71, p. 102038, 2021.
- [32] O. Oktay, W. Bai, M. Lee, R. Guerrero, K. Kamnitsas, J. Caballero, A. de Marvao, S. Cook, D. O'Regan, and D. Rueckert, "Multi-input cardiac image super-resolution using convolutional neural networks," in *International conference on medical image computing and computer-assisted intervention*. Springer, 2016, pp. 246–254.
- [33] C. H. Pham, A. Ducournau, R. Fablet, and F. Rousseau, "Brain mri super-resolution using deep 3d convolutional networks," in *IEEE International Symposium on Biomedical Imaging*, 2017.
- [34] D. Zhu and D. Qiu, "Residual dense network for medical magnetic resonance images super-resolution," *Computer Methods and Programs in Biomedicine*, 2021.
- [35] S. You, B. Lei, S. Wang, C. K. Chui, A. C. Cheung, Y. Liu, M. Gan, G. Wu, and Y. Shen, "Fine perceptive gans for brain mr image super-resolution in wavelet domain," *IEEE Transactions on Neural Networks and Learning Systems*, 2022.
- [36] Y. Zheng, Y. Yang, T. Che, S. Hou, W. Huang, Y. Gao, and P. Tan, "Image matting with deep gaussian process," *IEEE Transactions on Neural Networks and Learning Systems*, 2022.
- [37] A. Levin, D. Lischinski, and Y. Weiss, "A closed-form solution to natural image matting," *IEEE transactions on pattern analysis and machine intelligence*, vol. 30, no. 2, pp. 228–242, 2007.
- [38] S. G. Armato III, G. McLennan, L. Bidaut, M. F. McNitt-Gray, C. R. Meyer, A. P. Reeves, B. Zhao, D. R. Aberle, C. I. Henschke, E. A. Hoffman *et al.*, "The lung image database consortium (lidc) and image database resource initiative (idri): a completed reference database of lung nodules on ct scans," *Medical physics*, vol. 38, no. 2, pp. 915–931, 2011.
- [39] K. Yan, X. Wang, L. Lu, and R. M. Summers, "DeepLesion: automated mining of large-scale lesion annotations and universal lesion detection with deep learning," *Journal of Medical Imaging*, vol. 5, no. 3, pp. 1 – 11, 2018.
- [40] S. Woo, J. Park, J.-Y. Lee, and I. S. Kweon, "Cbam: Convolutional block attention module," in *Proceedings of the European conference on computer vision (ECCV)*, 2018, pp. 3–19.
- [41] K. He, X. Zhang, S. Ren, and J. Sun, "Deep residual learning for image recognition," in *Proceedings of the IEEE conference on computer vision and pattern recognition*, 2016, pp. 770–778.
- [42] A. Paszke, S. Gross, F. Massa, A. Lerer, J. Bradbury, G. Chanan, T. Killeen, Z. Lin, N. Gimelshein, L. Antiga *et al.*, "Pytorch: An imperative style, high-performance deep learning library," *Advances in neural information processing systems*, vol. 32, 2019.
- [43] F. Milletari, N. Navab, S.-A. Ahmadi, and and, "V-net: Fully convolutional neural networks for volumetric medical image segmentation," in *2016 Fourth International Conference on 3D Vision (3DV)*, 2016, pp. 565–571.
- [44] M. Mirza and S. Osindero, "Conditional generative adversarial nets," *arXiv preprint arXiv:1411.1784*, 2014.
- [45] D. P. Kingma and J. Ba, "Adam: A method for stochastic optimization," *arXiv preprint arXiv:1412.6980*, 2014.
- [46] T. Kubota, A. K. Jerebko, M. Dewan, M. Salganicoff, and A. Krishnan, "Segmentation of pulmonary nodules of various densities with morphological approaches and convexity models," *Medical Image Analysis*, vol. 15, no. 1, pp. 133–154, 2011.
- [47] A. Cardona, S. Saalfeld, S. Preibisch, B. Schmid, A. Cheng, J. Pulokas, P. Tomancak, and V. Hartenstein, "An integrated micro-and macroarchitectural analysis of the drosophila brain by computer-assisted serial section electron microscopy," *PLoS Biol*, vol. 8, no. 10, p. e1000502., 2010.
- [48] G. Litjens, R. Toth, W. van de Ven, C. Hoeks, S. Kerkstra, B. van Ginneken, G. Vincent, G. Guillard, N. Birbeck, J. Zhang *et al.*, "Evaluation of prostate segmentation algorithms for mri: the promise12 challenge," *Medical image analysis*, vol. 18, no. 2, pp. 359–373, 2014.
- [49] C.-H. Yeh, C.-H. Lin, L.-W. Kang, C.-H. Huang, M.-H. Lin, C.-Y. Chang, and C.-C. Wang, "Lightweight deep neural network for joint learning of underwater object detection and color conversion," *IEEE Transactions on Neural Networks and Learning Systems*, 2021.
- [50] Y. Fu, S. Li, H. Zhao, W. Wang, W. Fang, Y. Zhuang, Z. Pan, and X. Li, "Elastic knowledge distillation by learning from recollection," *IEEE Transactions on Neural Networks and Learning Systems*, 2021.
- [51] A. Shamsi, H. Asgharnejhad, S. S. Jokandan, A. Khosravi, P. M. Kebria, D. Nahavandi, S. Nahavandi, and D. Srinivasan, "An uncertainty-aware transfer learning-based framework for covid-19 diagnosis," *IEEE transactions on neural networks and learning systems*, vol. 32, no. 4, pp. 1408–1417, 2021.
- [52] S. Li, M. Lin, Y. Wang, Y. Wu, Y. Tian, L. Shao, and R. Ji, "Distilling a powerful student model via online knowledge distillation," *IEEE Transactions on Neural Networks and Learning Systems*, 2022.
- [53] M. Zhu, J. Li, N. Wang, and X. Gao, "Knowledge distillation for face photo-sketch synthesis," *IEEE Transactions on Neural Networks and Learning Systems*, 2020.
- [54] P. Liu, W. Yuan, J. Fu, Z. Jiang, H. Hayashi, and G. Neubig, "Pre-train, prompt, and predict: A systematic survey of prompting methods in natural language processing," *arXiv preprint arXiv:2107.13586*, 2021.
- [55] D. Mellouli, T. M. Hamdani, J. J. Sanchez-Medina, M. B. Ayed, and A. M. Alimi, "Morphological convolutional neural network architecture for digit recognition," *IEEE transactions on neural networks and learning systems*, vol. 30, no. 9, pp. 2876–2885, 2019.
- [56] W. Xie, J. Lei, Y. Cui, Y. Li, and Q. Du, "Hyperspectral pansharpening with deep priors," *IEEE Transactions on Neural Networks and Learning Systems*, vol. 31, no. 5, pp. 1529–1543, 2019.